Mitochondrial haplotype and mito-nuclear matching drive somatic mutation and selection throughout aging

Isabel M. Serrano[1], Misa Hirose[2], Clint Valentine[3], Sharie Austin[3], Elizabeth Schmidt[3], Gabriel Pratt[3], Lindsey Williams[3], Jesse Salk[3], Saleh Ibrahim[4], and Peter H. Sudmant[1,5,6]

Affiliations
[1] Center for Computational Biology, University of California, Berkeley
[2] Lübeck Institute of Experimental Dermatology, University of Lübeck
[3] TwinStrand Biosciences
[4] College of Medicine, Khalifa University
[5] Department of Integrative Biology, University of California, Berkeley
[6] Corresponding Author

Abstract
Mitochondrial genomes co-evolve with the nuclear genome over evolutionary timescales and are shaped by selection in the female germline. Here, we investigate how mismatching between nuclear and mitochondrial ancestry impacts the somatic evolution of the mt-genome in different tissues throughout aging. We used ultra-sensitive Duplex Sequencing to profile ~2.5 million mt-genomes across five mitochondrial haplotypes and three tissues in young and aged mice, cataloging ~1.2 million mitochondrial somatic mutations. We identify haplotype-specific mutational patterns and several mutational hotspots, including at the Light Strand Origin of Replication, which consistently exhibits the highest mutation frequency. We show that rodents exhibit a distinct mitochondrial somatic mutational spectrum compared to primates with a surfeit of reactive oxygen species-associated G>T/C>A mutations and that somatic mutations in protein coding genes exhibit strong signatures of positive selection. Lastly, we identify an extensive enrichment in somatic reversion mutations that "re-align" mito-nuclear ancestry within an organism's lifespan. Together, our findings demonstrate that mitochondrial genomes are a dynamically evolving subcellular population shaped by somatic mutation and selection throughout organismal lifetimes.

Introduction

The mitochondrial genome (mt-genome) encodes for 13 proteins that are vital for the electron transport chain. However, more than 1,000 nuclear encoded genes are necessary for mitochondrial assembly and function[1]. The required coordination between nuclear- and mitochondrial-encoded proteins drives the coevolution of these two genomes[2–4]. This concerted evolution has been observed in both laboratory crosses and natural hybrids across a variety of species, including: fruit flies[5,6], marine copepods[7,8], wasps[9–11], yeast[12,13], eastern yellow robins[14], swordtail fish[15], and teleost fish[16]. Hybrids often exhibit reduced fitness attributed to attenuated mtDNA copy number[17], mtDNA gene expression[17,18], and OXPHOS function[6–8,10]. In natural hybrids, the genetic ancestry at nuclear-encoded mitochondrial genes is highly differentiated between populations that have distinct mt-haplotypes[14]. In human admixed populations, mito-nuclear ancestral discordance has been shown to correlate with reductions in mtDNA copy number[19]. Additionally, *de novo* germline mitochondrial mutations in admixed human populations exhibit a bias towards concordance with nuclear ancestry[20]. Together, these studies highlight the functional importance of mito-nuclear ancestral concordance. However, the impact of these genomic interactions on somatic mutation and selection has not been studied.

As healthy cells age, they accumulate nuclear and mtDNA damage as a result of environmental exposures and cellular processes[21]. mtDNA has a 10- to 100-fold higher *de novo* germline mutation rate than nuclear DNA[20,22,23] due to its lack of protective histones, a higher replication rate, and less effective DNA damage repair mechanisms[24]. Individual cells can contain hundreds to thousands of mt-genomes[25,26], presenting a dynamic subcellular population that is highly susceptible to mutation. While the relationship between mutations in the mt-genome and aging remains unclear[27,28], increased mtDNA damage has been associated with many aging phenotypes and several age-related diseases[27,29]. Yet, profiling low frequency mutations in this population of mt-genomes has historically been challenging with most technologies limited to variants segregating at a frequency >1%[23,30]. More recently, several studies have employed Duplex Sequencing[30] to capture mutations with an error rate of <1x10^{-7}. These works have examined several different species and confirmed a robust age-associated increase in mtDNA somatic mutation frequency[31–33], identified that DNA replication error is the predominant source of mitochondrial somatic mutation[31–34], and observed tissue-specific somatic mutation rates[33,34].

Here, we investigate the impact of mitochondrial ancestry (mt-ancestry) and tissue-type on the somatic evolution of the mt-genome through age. To explore how mitochondrial haplotype and mito-nuclear genomic interactions shape the mt-genome mutational landscape, we utilize a panel of mouse strains that have identical nuclear genomes but differ in their mitochondrial haplotypes (conplastic strains). We sample the brain, heart, and liver of these conplastic strains and the wildtype (C57BL/6J) in young and aged individuals. These tissues are physiologically distinct yet some of the most metabolically active allowing us to study how evolutionary processes unfold in different molecular contexts. We use Duplex Sequencing to profile mt-genomes at an unprecedented level of depth and accuracy, allowing us to identify mutational hotspots and characterize the mutational spectrum. We use these results to discern signatures of selection acting to shape the mt-genome through age and confirm the existence of somatic mutations that work to realign mito-nuclear ancestry at short, within-lifespan, evolutionary timescales. Together, these findings characterize somatic evolution in the context of an organelle implicated in aging and age-related phenotypes.

Results

Ultra-sensitive duplex sequencing of 2.5 million mitochondrial genomes allows profiling of mutations to a frequency of 4x10^{-6}

To investigate how mitochondrial haplotype and mito-nuclear concordance influence the distribution of mt-genome somatic mutations, we employed a panel of conplastic mouse strains. These strains are inter-population hybrids developed by crossing common laboratory strains with the C57BL/6J (B6) mouse line[35]. Each conplastic mouse strain carries a unique mitochondrial haplotype on a C57BL/6J nuclear genomic background **(Fig. 1 A)**. This fixed nuclear background enables us to attribute differences in somatic mutation to changes in mitochondrial haplotype. Alongside a wildtype B6 mouse, we used four conplastic mouse strains that exhibit changes in metabolic content and processes, or altered aging phenotypes **(Table S1)**. Three of these conplastic mouse strains differ from the C57BL/6J mitochondrial haplotype by just 1-2 nonsynonymous variants, while a single strain (NZB) contains 91 variants distributed across the mt-genome **(Fig. 1B, Table S1)**. We sampled brain, liver, and heart tissues from each of these mouse strains in young (2-4 months old (mo.)) and aged (15-22 mo.) individuals to examine how aging and metabolic demands shape the mutational spectrum in distinct physiological contexts. In total, three tissues were sampled from five mouse strains at two different ages over 3-4 replicates per condition, resulting in n=115 samples.

In order to capture low frequency variants and accurately portray the somatic mutational landscape, we used ultra-sensitive Duplex Sequencing to profile mt-genomes across different experimental conditions[30]. This approach works by tagging double stranded mtDNA sequences with molecular identifiers and computationally constructing a duplex consensus sequence **(Fig. 1C)** resulting in error rates of ~2 x 10^{-8}. Using this approach, we profiled ~2.5 million duplex mt-genomes, with a median of 74,764 duplex mt-genomes sequenced per condition (*strain x tissue x age*) **(Fig. 1D)**. This resource allows for the detection of somatic mutations at a frequency of 4x10^{-6}.

Duplex reads from each sample were mapped to the mouse mitochondrial genome (mm10) and variants were called using a Duplex Sequencing processing pipeline (see Methods). Mutations overlapping conplastic haplotype sites were filtered out. In total we identified 1,171,918 somatic variants, with a median of 40,449 somatic mutations per condition **(Fig. 1E).** These variants were distributed across the entirety of the mt-genome **(Fig. 1F)**.

Haplotype- and tissue-specific mitochondrial mutation rates and hotspots

Somatic mutations accumulate with age across both nuclear and mitochondrial genomes[21]. We observed this trend consistently across tissues and mt-haplotypes with the mutation frequency on average ~2-fold higher in aged mice compared to young mice **(Fig. 2A)**. This trend was most pronounced in the liver (2.5-fold higher) and smallest in the heart (1.6-fold higher). Additionally, the heart sustained the lowest mutation frequency on average **(Fig. 2A)**, despite its high metabolic demands. Comparing age-associated mutation rates across different strains we find AKR, ALR, and NZB all exhibit strain-specific mutation rates **(Table S2)**, p-value < 0.01: log-link regression). The FVB strain, which only differs from B6 at two sites **(Fig. 1B)** showed no evidence of strain-specific mutation rates compared to wildtype. AKR and ALR strains had lower mutation rates across all tissues while NZB exhibited strong increases in the brain and decreases in the heart.

We next examined the variation in mutation rates and frequencies across different regions of the mitochondrial genome **(Fig. 2B, C)**. The density of mutations was lowest in functional coding regions (protein coding, rRNA, and tRNA segments) while the *D-loop* exhibited a significantly higher mutation frequency in both young (6.4-fold, p-value = 3.4 x 10^{-9}; two-tailed t-test) and aged (4.5-fold, p-value = 8.6 x 10^{-8}; two-tailed t-test) mice. However, we further found that the light strand origin of replication (*OriL*) had an even higher average mutation frequency, 7- to 4-fold in excess of the D-loop in young and aged mice, respectively **(Fig. 2B)**. This *OriL* hotspot of mutation was most pronounced in aged wildtype B6 mice. The *OriL* was recently noted as a mutational hotspot in macaque liver, but not in oocytes or muscle in that species[33]. In contrast, we find the *OriL* to exhibit elevated mutation rates across all tissues examined in this study.

Our initial inspection of the overall distribution of mutations across the mt-genome highlighted several distinct clusters appearing at finer-scale resolution than our simple functional classification groups **(Fig. 1F).** To resolve these putative mutational hotspots we quantified the average mutation frequency in 150 base-pair (bp) sliding windows over the mt-genome independently across tissues and mt-haplotypes **(Fig. 3A)**. In addition to the *D-loop*, this analysis identified mutational hotspots in *OriL, mt-ND2*, and *mt-tRNA^Arg*.

The *OriL* forms a stem loop structure that is conserved across species[36] however differs markedly in its sequence. We identified mutations throughout the loop and 3` end of the stem with the highest mutation frequencies corresponding to changes in the size of the stem loop (**Fig. 3B**). Repeated mutations of the 3` end of the stem loop structure mirror those observed in macaque liver in a recent study[33], though the sequence of the stem differs between these two species. Thus, the conserved structure of the *OriL* appears to drive convergent mutational phenotypes between species.

The *mt-ND2* mutation hotspot consists of a frameshift-inducing A insertion or deletion that introduces a premature stop codon. This stop codon reduces the length of the final protein product by more than 250 amino acids, likely severely impacting its function. This mutation increases in frequency with age across all strains except NZB. The final mutation hotspot we identified is localized to an 8 nucleotide stretch of *mt-tRNA^Arg* (**Fig 3D**). These nucleotides correspond to the 5` D-arm stem-loop of the tRNA and constitute primarily A insertions 2-4 nucleotides long. Computational tRNA structure predictions show that these mutations increase the size of the loop **(Fig S.2, Fig S. 3)**. This mutational hotspot exhibits strong strain-specificity with B6 exhibiting few somatic mutations in this A-repeat stretch. The D-arm plays a critical role in creating the tertiary structure of tRNAs [37,38] potentially contributing to its constraint in the wildtype. Together, these results highlight the emergence of distinct mutational hotspots in mitochondrial genomes occurring in age- and strain- specific contexts, and implicating both DNA and RNA secondary structures.

DNA replication error and deletion events are distinguishing features of aged mitochondrial genomes

Somatic mutations are caused by various molecular processes that lead to DNA damage, each of which exhibit a distinct mutational signature[39]. To identify sources of mitochondrial somatic mutation, we categorized mutations into single nucleotide variants (SNVs), deletions (DEL) and insertions (INS) **(Fig. 4A)**. SNVs were further classified into the six possible substitution classes **(Fig. 4B)**. Overall, SNVs were the predominant somatic mutation type, with a 5-fold higher average mutation frequency than deletions and insertions in both young and aged individuals **(Fig S. 4)**. The most abundant mutation type observed was G>A/C>T, which is indicative of

replication error or cytosine deamination to uracil [40,41] **(Fig. 4B)**. The reactive oxygen species (ROS) damage signature of G>T/C>A[42] was the second most predominant mutation type. All somatic mutation types were used to identify two dominant mutational signatures using a multinomial bayesian inference model[43] **(Fig. 4C)**. These signatures explained the bulk of the variation across samples **(Fig S5)**.

The accumulation of somatic mutations with age is a well known phenomenon that has been hypothesized to play key roles in the etiology of lifespan[44]. We observed that 4 out of the 8 mutation types significantly increased in frequency with age (adjusted p-value < 0.01; Fisher's Exact Test with a Benjamini-Hochberg correction) **(Fig. 4B, Table S3)** across all tissues, with T>A/A>T mutations additionally exhibiting age-associated accumulation in the liver but not in brain or heart. These age-associated signatures compose *Mutational Signature B* **(Fig. 4C)**, which overall distinguishes aged from young samples **(Fig. 4D)**. The consistency of these signatures across both mutations and mt-haplotypes suggest that these mutations occur in a 'clock-like' fashion in mitochondria over lifespan.

In contrast, insertions, G>C/C>G, and G>T/C>A mutations did not exhibit consistent age-associated patterns. These mutations are represented in *Mutational Signature A* **(Fig. 4C)**. Of particular note, the G>T/C>A mutation pattern is associated with ROS damage. An increase in ROS damage has been hypothesized to play an important role in aging. Nonetheless, we do not find evidence of an increase in ROS-associated damage with age. Previous works in the human brain[31,45] and various mouse tissues[32] have also observed a lack of ROS-associated damage with age.

Evidence of distinct somatic mitochondrial mutational signatures across species

While the overwhelming majority of research into somatic mutation rates and profiles has focused on humans, comparative analyses can provide insight into the evolutionary processes that have shaped mutation. A recent cross-species comparison of nuclear somatic mutations in intestinal crypt cells, for example, found that the relative contributions of different mutational signatures varied among species[44].

To determine if mitochondrial somatic mutation exhibited species-specific patterns we compared several recent studies that Duplex Sequenced mt-genomes in multiple mouse, human, and macaque tissues[31–33]. In our dataset, we found the relative magnitude of mutation frequencies to be consistent across tissues and mt- haplotypes with the G>A/C>T and G>T/C>A mutations being the most abundant **(Fig. 4B, Fig S. 6A, Table S4).** This signature is consistent with other duplex sequencing-based analyses of mitochondrial mutations in young and aged mouse brain, muscle, and oocytes **(Fig. 4E, Fig S. 6B)**[32]. However, profiling of mitochondrial mutation signatures in several young and aged human brains noted transitions, G>A/C>T and T>C/A>G, to be the most abundant mutation signatures[31] **(Fig. 4E)**. We find that this pattern is also recapitulated in a recent dataset of mitochondrial somatic mutation in macaque muscle, heart, liver and oocytes (**Fig S. 6C, Table S4)**[33]. Together, these results suggest that rodent and primate mt-genomes are subject to distinct mutational processes, potentially as a cause or effect of physiological differences between these lineages.

Positive selection predominantly shapes the mutational landscape of the mt-genome

While only thirteen proteins are encoded on the mt-genome, these products are vital components of the electron transport chain. Given their importance, we investigated whether selection was acting to shape the mutational landscape of the mt-genome. Previous studies focused on *de novo* mutations in mice have not identified signals of selection[32]. However, it has been suggested that this may be due to the low frequencies of these variants, which prevents them from having a phenotypic effect on mitochondrial function. By contrast, studies focused on higher frequency mutations in humans, greater than 0.5% frequency, have identified both signals of positive[46] and negative selection[47]. In our analysis, we quantify selection using mutations with a frequency less than 1×10^{-3}, allowing us to characterize evolutionary processes acting on mutations that have not been previously well-documented.

To determine if selection was acting on the population of mt-genomes, we calculated the $\frac{hN}{hS}$ statistic[46], which is akin to the $\frac{dN}{dS}$ statistic, for every gene across our 29 experimental conditions. For each condition, we also simulated the expected distribution of $\frac{hN}{hS}$ ratios using the observed mutation counts and mutational spectra. From this analysis we observed that, on average, even simulations of random mutations were much more likely to exhibit signatures of positive selection than neutral or negative selection, due to the overall nucleotide makeup of the mt-genome and predominant mutation types (p-value < 2.2×10^{-16}; one sample t-test) **(Fig. 5A)**. Nonetheless, overall our observed $\frac{hN}{hS}$ statistics were enriched for stronger signatures of positive selection across conditions (p-value < 2.2×10^{-16}; Wilcoxon Rank Sum Test). On a gene-by-gene basis while the expected $\frac{hN}{hS}$ was consistently >1 (one sample t-test; adjusted p-value < 0.01 with Bejamini-Hochberg correction) 6 out of 13 individual genes exhibited signatures of positive selection in excess of expectation **(Fig. 5B,C)**. These signals of positive selection were predominantly seen for genes that compose Complex I and III of the electron transport chain (two sample t-test; adjusted p-value < 0.01 with Bejamini-Hochberg correction) **(Fig. 5C)**.

Across our 29 experimental conditions, we identified 67 cases of genes under selection (adjusted p-value <0.01) with a higher proportion of genes exhibiting positive selection (N=55) versus negative selection (N=12). On average, young and aged mice do not differ in the proportion of genes under selection nor in the strength of selection **(Fig. 5D)**. We also quantified the consistency of selection signatures across experiments and conditions. Strikingly, Complex I genes were found to be frequently under selection with mt-*ND1*, *2, 4,* and *5*, exhibiting signatures of positive selection in 21-41% of experiments **(Fig. 5E)**. Although we observed a bias towards positive selection across experimental conditions, *mt-Atp8* and *mt-ND3* predominantly undergo negative selection. Together, these results demonstrate that selection is pervasive in shaping the somatic mutational landscape of mt-genomes.

Somatic reversion mutations are highly enriched and increase in frequency with age

Mismatching of mitochondrial and nuclear haplotypes, such as in hybrid populations, has been associated with reductions in fitness[5–13,15]. Given the constant collaboration between mitochondrial and nuclear genomic products, the mt-genome must co-evolve with the nuclear genome in order to maintain mitochondrial function. Yet, observing evolutionary processes that act to increase mito-nuclear matching is challenging. The conplastic strains we employ are

hybrids with mismatched nuclear and mt-genome ancestries. Since hybrids often demonstrate reduced fitness as a result of mito-nuclear discordance, we reasoned that at sites where the conplastic mt-genome differed from the B6 mt-genome (haplotype sites), there may be a preference for "reversion" mutations to the B6 allele **(Fig. 6A)**.

We hypothesized that if somatic selection were to favor the B6 allele, then reversions would occur at a higher rate than background mutations. Three of the strains have several fixed haplotype sites in their mitochondrial genomes, ALR, FVB, and NZB. We find that in ALR and FVB strains, haplotype sites were among the most mutated sites in the mt-genome, with 6-fold and 7-fold higher average mutation frequency than non-haplotype sites, respectively (**Fig. 6B,** adjusted p-values <0.001**)**. In NZB, which differs from B6 at 91 locations, these haplotypes sites had 122-fold higher mutation frequency than background (adjusted p-values $<1x10^{-53}$). The overwhelming majority (75% - 100%) of these mutations are reversions to the B6 allele with the specific reversion mutation occurring significantly more than expected by chance **(Table S5)**. These results demonstrate the extreme selective pressures impressed by nuclear-mitochondrial matching to reintroduce the ancestral allele.

We next hypothesized that if somatic selection were to favor reversions, these B6 reversion alleles should increase in frequency with age. We quantified the relative change in reversion frequencies across strains and found that in ALR and FVB all unique fixed sites exhibited a significant increase in the reversion allele frequency with age across all tissues (**Fig 6C**, **Table S6,** BH adjusted p-value < 0.01**)**. This suggests a strong benefit of these coding reversion substitutions in ALR and FVB strains. In contrast, in NZB we observed an overwhelming preference for reversion alleles to decrease in frequency with age, particularly in the brain **(Fig 6C., Table S6)**. One potential explanation for this decrease in frequency compared to ALR and FVB is that the many NZB fixed substitutions exhibit epistatic interactions which manifest negatively if single reversions are not accompanied by mutations at other sites, though this is challenging to test. We did identify two cases in NZB of reversions that increase in frequency with age, a synonymous substitution in the *mt-CO2* gene, and a noncoding mutation in the *D-loop*. Together, our results demonstrate that sites which contribute to mito-nuclear mismatching are prone to elevated levels of mutation with reversion alleles preferred across multiple tissues in populations. This preference for nuclear mitochondrial matching potentially drives somatic selection increasing the frequency of these alleles with age.

Discussion

The interdependence of nuclear- and mitochondrially-encoded genes has significantly shaped patterns of diversity and constraint on these two genomes across organisms and populations. Yet, the mt-genome also exhibits exceptionally high somatic mutation rates and is thus dynamic within individuals' lifespans. Here, we explored the relationship between nuclear-mitochondrial ancestral matching and the accumulation of somatic mutations. Our results extended upon other works that employ highly sensitive Duplex Sequencing to characterize the mutational landscape of the mt-genome [31–33] and generated, to our knowledge, the largest mt-genome somatic mutational catalog to date. We profiled 2.5 million mt-genomes across 4 conplastic mouse strains and the B6 wildtype, with a median of more than 74,000 mt-genomes per biological condition. Our results corroborated other studies of somatic mutation in the mt-genomes of mice, humans, and macaques, which demonstrate an age-associated increase in mutations as well as tissue-specific mutation rates. Our study design also uniquely allowed us to additionally assess the role of mt-haplotype on mutation rates. The conplastic strains employed each exhibit distinct physiological differences which likely play a role in modulating mutations. We find cases

in which mt-haplotype impacts mitochondrial mutation rate, which emphasizes that specific fixed substitutions between mitochondrial haplotypes can play a vital role in shaping mutational profiles.

Our high duplex coverage allowed us to characterize mutational hotspots throughout the mt-genome at fine-scale resolution. As expected, the *D-Loop* had a high mutation frequency compared to other regions in the genome. However, we identified three additional hotspots exhibiting either age- or haplotype-associated mutation frequencies. The first of these hotspots occurs in the *OriL,* the light strand origin of replication, which forms a DNA stem-loop structure. While the sequence of this region is highly divergent among species, the structure is conserved. Recently, Arbeithuber et al. [33] identified the *OriL* as a hotspot of mutation in macaque liver. We similarly find mutations at this locus to be most prominent in aged wild-type liver, however our increased sequencing depth allows us to show that this is a consistent hotspot across tissues and strains regardless of age. We identify mutations in both the stem and the loop of this structure, with mutations occurring in the same 5' end of the stem as those identified in macaque, albeit impacting completely different sequences. These results highlight that the conserved structure of this stem loop is sensitizing to conserved mutational patterns across species. Similarly, peaks of mutation frequency within the *D-Loop* have been narrowed to regions associated with mtDNA replication[20,46,48]. The mutational hotspots surrounding mtDNA origins of replication have been hypothesized to serve as a compensatory mechanism against mutation by slowing mtDNA replication[33]. We identified an additional hotspot occurring in a highly structured nucleic acid, *mt-tRNA^Arg*. Intriguingly, these mutations are only found in conplastic strains, suggesting that they are poorly tolerated in the wildtype. These mutations are expected to increase the size of the loop in the 5` D-arm stem-loop of this tRNA. Polymorphisms that increase the size of the D-arm in *mt-tRNA^Arg* have been linked with an increase in mtDNA copy number triggered by heightened reactive oxygen species production[49]. Specifically, the size of the loop, not the underlying sequence, was found to be important for mitochondrial function[38]. Together, these findings suggest that mutational hotspots in the mt-genome may potentially act as compensatory mechanisms to alter mtDNA replication and copy number.

While Duplex Sequencing approaches have allowed us to identify DNA replication error as the primary driver of somatic mutations in mitochondria[31–33], the full extent of mutational processes impacting mt-genomes remains unknown. Recent studies have determined that different species exhibit varying contributions of mutational signatures in the nuclear genomes of aging intestinal crypt cells[44]. Comparing the mutational spectra across several studies that duplex-sequence the mt-genomes of humans, mice, and macaques in various tissues, we similarly find that rodents exhibit distinct mutational profiles compared to primates. Although DNA replication error is the predominant mutation type across species, rodents exhibit a surfeit of G>T mutations in contrast to primates. While studies in humans previously concluded that transitions are the most common mutation in mitochondria, we find that the abundance of the T>C marker of DNA replication error is a species-specific effect. We are not able to determine whether this finding is the result of physiological differences between these organisms, or variability in the repair pathways of these species. Of note, we find these trends hold both for somatic mutations as well as de-novo oocyte mutations in the mt-genome, suggesting that the underlying mechanisms driving these distinct profiles have potentially shaped patterns of mt-diversity across different species. These findings recapitulate that distinct life history traits impact the evolution of the mt-genome across species. Compared to primates, rodents have a shorter lifespan and a substantially smaller body size. The difference in G>T mutations, which are associated with reactive oxygen species damage, and T>C mutations, a marker of DNA replication error, suggest that repair mechanisms or ROS defenses may differ between these species. Further analyses across a broad range of species, such as those recently performed in

the nuclear genome[44], are needed to inform how mitochondrial mutational processes are specifically associated with disparate life histories.

Mitochondrial genomes exist as a population inside cells, where selection can act to shape this population across various biological scales. In oocytes, strong genetic drift induced by the mitochondrial genetic bottleneck[23] and purifying selection[20,50] have been shown to shape the transmission of mt-genome mutations across generations. In somatic tissues, the population of mt-genomes may be shaped at the cellular level, as a result of inter-cellular competition; at the inter-mitochondrial level, with mitochondrial turnover; or at the intra-mitochondrial level between mt-genomes harboring different variants. We determine that the mutational spectrum of mt-genomes predisposes to signatures of positive selection, as quantified by the proportion of nonsynonymous to synonymous mutations observed. Nonetheless, the observed rate of non-synonymous mutations was even higher than would be expected by chance, indicating that positive selection is pervasive at the somatic scale. This was consistent across strains however the wildtype exhibited the highest proportion of genes under negative selection, as might be expected for matched nuclear-mitochondrial haplotypes. Genes that compose Complex I and Complex III of the electron transport chain (ETC) were significantly enriched for positive selection. These complexes are hypothesized to be the primary source of reactive oxygen species production in the ETC, where a severe abundance of reactive oxygen species has been linked to several age-related diseases[51,52]. In contrast to the germline, the mt-genome is predominantly shaped by positive selection in somatic tissues; yet, the effects that these mutations have at the mitochondrial and cellular level along with the advantages these mutations confer remains to be explored.

Our study also allowed us to examine a very specific form of somatic selection: the emergence and persistence of reversion mutations that re-match the mitochondrial haplotype to its nuclear constituent. Previously, Wei et al. identified the preferred maternal transmission of variants that worked to re-align mitochondrial and nuclear ancestry in humans[20]. This result showcased that selection for reversions can occur in as short as one generation, emphasizing the strong influence mito-nuclear interactions have in shaping mt-genome diversity. We find selection for reversion mutations at even shorter timescales: within an organism's lifespan. These mutations are extremely abundant, much more than expected by chance, and in several cases increase in frequency with age. Importantly, the change in reversion allele frequencies with age was dependent on the genetic divergence between the mitochondrial and nuclear ancestries. That is, mice with the greatest genetic divergence from the B6-mitochondrial haplotype observed the opposite trend, a decrease in reversion frequency with age. Despite mito-nuclear ancestral mismatching, NZB mice did not showcase phenotypic differences compared to B6[53]. Thus, understanding to what extent mito-nuclear matching influences somatic evolution remains to be explored. Altogether, these observations highlight a hitherto unexplored impact of mito-nuclear incompatibility, namely its potential role on the somatic evolution of tissues.

While we sequence to great depth across various tissues, we are unable to characterize the impact that cell-type plays on the evolution of the mt-genome. This analysis is of particular interest in tissues such as the heart and the brain which consist of both mitotic and post-mitotic cellular populations. Given that DNA replication error is a predominant age-associated mutational signature, sequencing at the single cell level will be pivotal in understanding the role that cell proliferation has on mitochondrial somatic mutation. Additionally, our study only examined the wildtype B6 mouse and conplastic strains with nuclear B6 backgrounds. Reciprocal conplastic strains, in which both mitochondrial haplotypes are placed in the context of both nuclear genomes, will allow us to parse apart the different roles that the nuclear and mitochondrial genomes have in driving distinct mutational processes. Lastly, our study

emphasizes the importance of comparative somatic mutation profiling in order to discern how processes that shape mutation in the mt-genome differ with life history traits. Altogether, our findings explore somatic evolution in the context of an important cellular organelle and begin to discern the various scales at which evolutionary processes act to shape the population of mt-genomes.

Methods

Ethics Statement

Animal use and all methods were approved by the Animal Care and Use Committee (V242-7224. 122-5, Kiel, Germany). Experiments were performed in accordance with the relevant guidelines and regulations by certified personnel.

Data collection

The wildtype C57BL/6J (B6) and inbred mouse strains were obtained from Jackson Laboratory and maintained at the University of Lübeck. Conplastic strains B6-mtAKR, B6-mtALR, B6-mtFVB, and B6-mtNZB were generated and bred as described in[35] at the University of Lübeck. Briefly, the conplastic strains were developed by crossing female mice from AKR, ALR, FVB, and NZB mouse strains with male B6 mice. Female offspring were then backcrossed with male B6 mice. After the tenth generation of backcrossing mice were deemed conplastic mice with a B6 nuclear background and their respective maternal mitochondrial haplotypes. The brain, heart, and liver were sampled from young (2-4 months old (mo.)) and aged (15-22 mo.) mice in each strain (n = 115). B6 young liver samples and one B6 young heart sample were omitted from the data due to possible contamination **(Fig S1)**. Samples were validated by checking for their defining haplotype sites **(Table S1).**

Sequencing

Duplex sequencing libraries were prepared by TwinStrand Biosciences (Seattle, WA) as previously described[30,31]. Sequencing was performed at the University of California, Berkeley using Illumina NovaSeq generated 150 bp paired-end reads.

Data processing

Sequencing reads were processed into Duplex Sequencing reads and mapped to the reference mouse mitochondrial genome (mm10) using a modified version of the Duplex Sequencing processing pipeline developed by Dr. Scott Kennedy's group at the University of Washington, Seattle. The pipeline was edited to take as input bam files formed from the NovaSeq reads using bwa mem and is available on our github. Software versions used along with all processing steps including duplex consensus sequencing generation, mapping, and variant calling can be found in the github repository referenced below.

Mutational Signature Extraction

Observed counts for each mutation type (excluding mutations at a frequency > 1×10^{-3}) were used as input for sigfit (v 2.2), which is an R package used to identify mutational signatures. Sigfit uses Bayesian probabilistic modeling to uncover mutational signatures, as explained by Gori and Baez-Ortega[43]. Specifically, we use multinomial models to extract our signatures,

which is akin to the traditional non-negative matrix factorization approaches. The optimal number of signatures was determined by extracting a range of 1-7 signatures and comparing the cosine similarity **(Fig S5)** for this range (iterations = 1000, seed = 1756). The model was then refitted with two signatures, as determined by the goodness of fit test, with 10,000 iterations (seed = 1756).

Testing for selection

The number of nonsynonymous variants per nonsynonymous sites (hN) and synonymous variants per synonymous sites (hS) were calculated as described in [32,46]. The $\frac{hN}{hS}$ statistic was then quantified for each gene across the 29 experimental conditions. To test if the observed $\frac{hN}{hS}$ statistics were significant signals of selection, we used a multinomial distribution to simulate mutations for all experimental conditions using the observed mutation counts and proportions for each mutation type. The mutations were sampled across the mt-genome and the simulated $\frac{hN}{hS}$ statistics were calculated for each gene. 10,000 simulations were conducted for each experimental condition, where $\frac{hN}{hS}$ statistics that could not be calculated (hS = 0 or hN = 0) were excluded from the analysis. Mutations with a frequency > 1×10^{-3}, representing heteroplasmies, were excluded from the mutation count and proportions for each mutation type. Empirical p-values were used to determine if an observed $\frac{hN}{hS}$ statistic significant. The empirical p-value was calculated as the number of simulated $\frac{hN}{hS}$ statistics with a more extreme value than the observed $\frac{hN}{hS}$ statistic divided by the total number of simulated statistics. These empirical p-values were multiplied by a factor of 2 in order to account for both tails of the distribution. $\frac{hN}{hS}$ statistics with a Benjamini-Hochberg adjusted p-values < 0.01 were denoted as significant, where $\frac{hN}{hS}$ > 1 signified that a gene was under positive selection and $\frac{hN}{hS}$ < 1 suggested a gene was under negative selection.

Estimation of and correction for NUMT contamination

We originally mapped duplex paired end reads to a *mm10* masking the known NUMT region. We reasoned that given the 10-100-fold higher somatic mutation rate of the mitochondrial genome along with its several-hundred fold increased copy number with respect to the nuclear genome, that nuclear contaminating reads contribute minimally to our mutation frequencies. However, this low-level of contamination can potentially cause an issue when examining reversion mutations which are expected to be enriched for B6 allele in the NUMT.

To estimate and correct for this NUMT contamination, duplex paired end reads were remapped to mm10 using *bwa mem*. For this remapping, the NUMT region in chr1 (nt24611535 to nt24616184) was unmasked. The duplex read depth at junction regions, which captured sequences 10 bp upstream and 10 bp downstream of the NUMT region in chr1 and the corresponding region in the mt-genome (nt6394 to nt11042), was calculated using *samtools depth {input.in1} -b {input.in2} > {output}*. These junction regions contain sequences unique to chr1 and chrM, allowing us to estimate the % of reads mapping to ch1 as the number of reads mapping to chr1 divided by the average duplex depth of the mt-genome calculated with the chr1 NUMT masked **(Fig S7A).**

To validate this estimated contamination, we remapped the duplex paired end reads to the NZB reference genome (generated using an in-house script). The NZB mt-genome and B6 NUMT region differ by 24 SNVs. To map the duplex reads to the NUMT region we used *samtools depth {input.in1} -bq 30 {input.in2} > {output}*, setting a strict mapping quality score given that reads may differ from the regions by as few as 2 positions. Six regions across the NUMT were identified as having multiple SNVs within a read (<130 bp apart), which we refer to as SNV clusters. We used these clusters to identify reads that mapped to chr1. The estimated % of NUMT contamination at each SNV cluster was calculated as the number of reads mapping to chr1 divided by the average duplex depth of the mt-genome calculated with the chr1 NUMT masked. The estimated % of contamination at the junction regions was compared to the distribution of estimated % of contamination for the SNV clusters in NZB **Fig S7B).** The maximum estimated % of contamination between the junction regions was consistently equal to the median estimated % of contamination for the SNV clusters in NZB, verifying the consistency of the estimated % of NUMT contamination.

We take as a conservative measure the maximum estimated % of contamination from the junction regions **(~0.5% contamination**). The estimated chr1 read depth was then calculated as the original average mt-genome duplex depth multiplied by the estimated % of contamination. We calculated the corrected duplex mt-genome read depth in this region as the original duplex mt-genome read depth subtracted by the estimated chr1 read depth count. Likewise, the reversion allele depth is calculated as the original reversion allele count subtracted by the estimated chr1 read depth, assuming all reads from chr1 contain the B6 allele.

Statistical analysis: Testing for significance

Statistical analyses were performed using R (4.1.2). Poisson confidence intervals for average mutation frequencies were calculated using the *qchisq* function from the *stats* package in R (v 4.1.2). Log-link regressions were performed to determine an age-associated change in mutation frequency and mt-haplotype specific mutation rates (*glm, stats* package). Associations between (1) mutation type and age and (2) reversion allele and haplotype site were determined via Fisher's exact tests (*fisher.text, stats* package). To compare (1) the average mutation frequencies between the D-Loop and other regions in the mt-genome and (2) the average mutation frequencies of simulated and observed $\frac{hN}{hS}$ statistics on a gene-by-gene basis we used two tailed t-tests (*t.test, stats* package). To determine that our simulated $\log10(\frac{hN}{hS})$ > 0 altogether and in a gene-by-gene analysis we used a one-sample t-test (*t.test, stats* package). To compare (1) the average $\log10(\frac{hN}{hS})$ between our simulated and observed data and (2) background to haplotype site mutation frequencies for the NZB conplastic strain, we conducted Wilcoxon-Rank Sum tests (*wilcoxon.test, stats* package). Lastly, we calculate empirical p-values to determine the significance of observed $\frac{hN}{hS}$ statistics; high haplotype site mutation frequencies for AKR, ALR, and FVB; and for changes in mutation frequency with age for all haplotype sites. The empirical p-values are calculated as the number of simulated $\frac{hN}{hS}$ statistic (for 1) or number of background sites (for 2 and 3) with a more extreme value than our observed $\frac{hN}{hS}$ statistic (for 1), haplotype site mutation frequency (for 2), or change in mutation frequency for the haplotype site (for 3), divided by the total number of simulations (for 1) or total number of background sites (for 2 and 3). Multiple hypothesis test corrections were performed using the Benjimi-Hochberg correction (*p.adjust, stats* package), adjusted p-values refer to p-values that have undergone multiple hypothesis correction.

Data availability

All raw data has been uploaded to sequence read archive (accession pending). Processed duplex reads are deposited in zenodo.

Code availability

All code have been deposited in github (https://github.com/sudmantlab/conplastic_mt_profiling) with the repository archived in zenodo at (accession pending).
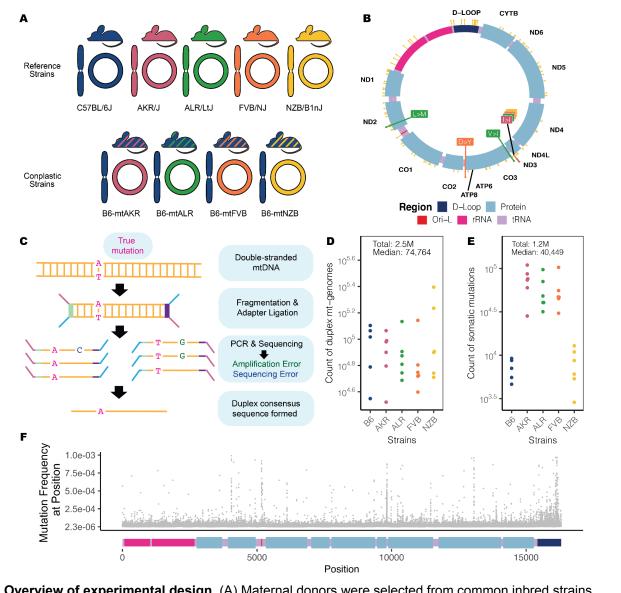
Author contributions

Conceived the experimental design: PHS.
Constructed the conplastic strains and provided experimental samples: MH and SI.
Sequencing design and library preparation: CV, SA, ES, GP, LW, JS.
Processed and analyzed the data: IMS and PHS.
Wrote and edited the manuscript: IMS and PHS.

Funding

Figures

Figure 1

Overview of experimental design. (A) Maternal donors were selected from common inbred strains (CISs) containing nonsynonymous variants with functional effects. Females from these CISs (pink, green, and orange) were backcrossed with a C57BL/6J mouse (blue). This process was repeated with a wild-inbred strain (yellow). The result of these crossings are conplastic mouse strains (denoted by the striped mice). These conplastic strains have identical B6 nuclear (linear) genetic backgrounds but differ by variants along their mt-genomes (circular). (B) B6-mtAKR (pink), B6-mtALR (green), and B6-mtFVB (orange) differ from wildtype by 1-3 missense variants. B6-mtNZB (yellow) contains 91 variants distributed across the mt-genome (14 missense and 56 synonymous mutations). The synonymous mutation in *mt-ND3* is shared across conplastic strains. For a more detailed account of these variants and their associated phenotypes reference **(Table S1)**. (C) Ultra-sensitive Duplex Sequencing (DupSeq) was used to profile mt-genomes from conplastic mice. DupSeq has an unprecedented error rate of $<10^{-7}$. Each double-stranded mtDNA fragment is distinctly tagged with a unique molecular

barcode, allowing for the computational construction of a duplex consensus sequence. As a result, both PCR and sequencing errors are filtered from the data. (D) The count of duplex mt-genomes sequenced was calculated for each experimental condition (n = 29 conditions; n = 4 mice for every condition with 3 mice for B6-Young-Heart). The duplex read depth at each position was aggregated across samples in a condition to quantify the duplex depth per condition. The average duplex read depth across the mt-genome was then calculated. An estimated 2.5 million mt-genomes were duplex sequenced with a median of 74,764 mt-genomes duplex sequenced per condition. (E) Approximately 1.2 million somatic variants were identified with a median of 40,449 variants per condition. The count of somatic variants was aggregated across samples in a condition. Mutations present at conplastic haplotype sites were filtered from the analysis. (F) The mutation frequency for each position is mapped along a linear representation of the mt-genome. Each point denotes the mutation frequency for an experimental condition at the given position in the mt-genome. Legends for the mt-genome map are consistent with those in **(Fig. 1B)**. Positions with a mutation frequency greater than 1×10^{-3} were excluded from this analysis.

Figure 2

Region-specific changes in somatic mutation frequency with age. (A) The average mutation frequency for each experimental condition. The mutation frequency for each position along the mt-genome was calculated by dividing the total count of alternative alleles by the duplex read depth at the position. Error bars denote the 95% Poisson confidence intervals. P-values indicate experimental conditions with a significant age-associated increase in somatic mutation frequency (log-linear regression and adjusted p-values using a Bonferroni multiple hypothesis correction). (B) The mt-genome was categorized into regions: OriL (red), D-Loop (dark blue), tRNAs (purple), protein coding (light blue), and rRNAs (magenta). For each region, the probability of mutation was calculated as the total count of mutations normalized by the region length in bp multiplied by the average duplex read depth across the region. Fill indicates age group: young (hollow circles) and aged (filled circles). (C) The difference in percent bp mutated between young and aged mice. The shape denotes the average difference in percent bp mutated with age across conditions. Error bars showcase the standard error of the mean. Positions that exceeded a mutation frequency of 1x10^{-3} were excluded from these analyses. For Fig. 2B and 2C, frequencies were normalized for sequencing depth across conditions at each position.

Figure 3

Haplotype-specific peaks of mutation along the mt-genome. (A) The average mutation frequency was calculated in 150-bp sliding windows for each strain and tissue independently. Each line represents a tissue: brain (blue), heart (red), and liver (orange). Regions with shared mutation frequency peaks in at least three mouse strains are labeled. (B) The high frequency region in OriL is highlighted. For positions 5171-5181 the mutation frequency for the T-repeat region is calculated as the sum of mutations across this region divided by the sum of the duplex depth across positions. Each

color denotes a different strain: B6 (blue), AKR (pink), ALR (green), FVB (orange), NZB (yellow). The average frequency in young (left, hollow points) and aged (right, filled points) mice are compared. The schematic compares the *OriL* structure in mice to that of macaques[33]. Positions with a mutation frequency > 1×10^{-3} are in magenta, while positions that undergo mutations are denoted in light blue. In the macaque *OriL* diagram, variant hotspots are denoted in light blue. Stars represent strains that have mutations present at a given position. (C) The high frequency region in *mt-ND2* is highlighted. Color, shape, and calculation of the average mutation frequency are similar to those in **Fig. 3B.** A schematic demonstrating the sequence and codon change that result from the indels at position 4050: a premature stop codon in the mutated sequences. The superscript denotes the position of the premature stop codon in the amino acid sequence. (D) The mutation frequency for *mt-tRNA^{Arg}* from bp positions 9820-9827, which is an A-repeat region. The mutation frequency for the A-repeat region is calculated as the sum of mutations across this region divided by the sum of the duplex depth across positions. The diagram of *mt-tRNA^{Arg}* highlights in magenta the location of a fixed variant in NZB and a high heteroplasmic variant in the other mouse strains. Positions that have mutations in this region are in light blue. Positions that exceeded a mutation frequency of 1×10^{-3} were excluded from these analyses. Frequencies were normalized for sequencing depth across conditions at each position.

Figure 4

Characterizing the mt-genome mutational landscape. (A) The average mutation frequency is compared between mt-haplotypes for different classes of mutations: single nucleotide variants (SNVs), deletions, and insertions. The average mutation frequency was calculated as the total mutation count in a class divided by the total duplex bp depth. Results for the brain are featured, which showcase trends observed in the heart and liver, as well **(reference Fig S4)**. (B) SNVs were further classified into point mutation types. The average mutation frequency for each mutation type was compared across mouse strains. The average frequency for point mutations was calculated as the total count of mutations of the given type divided by the duplex bp depth for the reference nucleotide. The average mutation frequency for deletions and insertions was calculated as the total mutation count in these classes divided by the total duplex bp depth. Mutation types are ordered by descending mutation frequencies. The range in frequency across experimental conditions for each mutation type is illustrated by the line segments and compared across age groups. Each point in the segment denotes the median frequency across conditions. (C) Mutational signatures were extracted from mutation type counts for each experimental condition using sigfit. Two mutational signatures were identified. The probability that a

mutation type contributed to a signature is showcased with error bars denoting the 95% confidence interval of each probability. (D) The presence of the mutational signatures was estimated for each condition (Signature A dark blue, Signature B light blue). The contribution of each mutational signature is compared across age. (E) The frequency of the three most abundant mutation types were compared across mice, macaques, and humans for the brain and liver. Mutation frequencies were normalized by the frequency of the G>A/C>T mutation in their respective study. All studies used Duplex Sequencing to profile mutations in the mt-genome. For the mutation frequencies in our study, we calculate the average mutation frequency across all strains. For all analyses, mutation counts and duplex bp depth were aggregated across samples in an experimental condition. Positions with mutation frequencies greater than 1×10^{-3} were omitted from these analyses.

Figure 5

Genes encoded on the mt-genome primarily undergo positive selection. (A) The distribution of observed $\frac{hN}{hS}$ statistics (white, N = 372) compared to the distribution of simulated $\frac{hN}{hS}$ statistics (gray; N = ~3.89 M). $\frac{hN}{hS}$ statistics that could not be calculated due to a lack of synonymous or nonsynonymous mutations were filtered from the analysis. Split violins show the distribution of the $\frac{hN}{hS}$ statistics while boxplots denote the median and quantiles of the distributions. The gray, dashed line highlights the neutral $\frac{hN}{hS}$ statistics in log10 scale. (B) For each gene, the distribution of observed $\frac{hN}{hS}$ statistics (white) is compared to the distribution of simulated $\frac{hN}{hS}$ statistics (gray). Split violins show the distribution of $\frac{hN}{hS}$ statistics while red diamonds highlight the average $\frac{hN}{hS}$ statistic in each distribution. Points denote observed $\frac{hN}{hS}$ statistics, with filled points highlighting significant signals of selection. Color represents each mouse strain: B6 (blue), AKR (pink), ALR (green), FVB (orange), NZB (yellow). The gray, dashed line denotes the neutral $\frac{hN}{hS}$ statistics in log10 scale. Genes are grouped by the electron transport chain complexes that their protein products correspond to. (C) The difference in average $\frac{hN}{hS}$ statistics

between the observed and simulated data. Asterisks denote genes in which there is a significant difference between the averages (two-sample t-test with a Benjimini-Hochberg correction; adjusted p-value < 0.01). Genes are grouped by the electron transport chain complexes that their protein products correspond to. (D) The average proportion of genes undergoing positive or negative selection across experimental conditions is compared between age groups. Additionally, the average strength of negative and positive selection across experimental conditions is compared between young and aged mice. Shading denotes age group: young (light gray) or aged (dark gray). Error bars denote the standard error of the mean. (E) The frequency for which a gene is under selection across experimental conditions. Genes are ordered by descending frequency. Color indicates the protein complexes that the gene products correspond to in the electron transport chain. The gray, dashed line denotes the neutral $\frac{hN}{hS}$ statistics in log10 scale. Proportions below the line indicate the frequency of genes under negative selection while proportions above the line indicate the frequency of genes under positive selection.

Figure 6

Somatic reversion mutations segregate in the mt-genome population. (A) A schematic that explains somatic reversion mutations. The wildtype strain (B6) has matching nuclear and mt-genome ancestries (B6 ancestry denoted in blue). Conplastic strains are hybrids with mismatching nuclear and mt-genome ancestry. Haplotype sites are positions in the mt-genome where the conplastic mt-genome differs from the B6 mt-genome. Somatic reversion mutations refer to the reintroduction of B6 ancestral alleles at haplotype sites. (B) The mutation frequency at non-haplotype sites (gray distributions) is compared to the mutation frequency at haplotype sites (green distributions or points when less than three haplotype sites exist). All mutations were included in the distribution of non-haplotype site mutation frequencies, including positions with a mutation frequency greater than 1×10^{-3}. Haplotype site mutation frequencies were corrected for potential NUMT contamination **(refer to Fig S7)**. Mutation frequencies were normalized for sequencing depth between young and aged experimental conditions. Denoted are the adjusted empirical p-value. Asterisks denote the number of haplotype sites with the same p-value. (C) A map of the somatic reversion mutations along a linear mt-genome. Each point denotes the change in frequency with age (delta) for a somatic reversion mutation. The size of the point indicates the magnitude of delta and color represents the conplastic strain the somatic reversion occurs in. Fill denotes significance (adjusted empirical p-value < 0.01).

References

1   Hill GE. Mitonuclear Compensatory Coevolution. *Trends Genet* 2020; **36**: 403–414.

2   Osada N, Akashi H. Mitochondrial-nuclear interactions and accelerated compensatory evolution: evidence from the primate cytochrome C oxidase complex. *Mol Biol Evol* 2012; **29**: 337–346.

3   Barreto FS, Burton RS. Evidence for compensatory evolution of ribosomal proteins in response to rapid divergence of mitochondrial rRNA. *Mol Biol Evol* 2013; **30**: 310–314.

4   Weaver RJ, Rabinowitz S, Thueson K, Havird JC. Genomic Signatures of Mitonuclear Coevolution in Mammals. *Mol Biol Evol* 2022; **39**. doi:10.1093/molbev/msac233.

5   Montooth KL, Meiklejohn CD, Abt DN, Rand DM. Mitochondrial-nuclear epistasis affects fitness within species but does not contribute to fixed incompatibilities between species of Drosophila. *Evolution* 2010; **64**: 3364–3379.

6   Meiklejohn CD, Holmbeck MA, Siddiq MA, Abt DN, Rand DM, Montooth KL. An Incompatibility between a mitochondrial tRNA and its nuclear-encoded tRNA synthetase compromises development and fitness in Drosophila. *PLoS Genet* 2013; **9**: e1003238.

7   Ellison CK, Burton RS. Disruption of mitochondrial function in interpopulation hybrids of Tigriopus californicus. *Evolution* 2006; **60**: 1382–1391.

8   Ellison CK, Burton RS. Interpopulation hybrid breakdown maps to the mitochondrial genome. *Evolution* 2008; **62**: 631–638.

9   Niehuis O, Judson AK, Gadau J. Cytonuclear genic incompatibilities cause increased mortality in male F2 hybrids of Nasonia giraulti and N. vitripennis. *Genetics* 2008; **178**: 413–426.

10   Ellison CK, Niehuis O, Gadau J. Hybrid breakdown and mitochondrial dysfunction in hybrids of Nasonia parasitoid wasps. *J Evol Biol* 2008; **21**: 1844–1851.

11   Koevoets T, Niehuis O, van de Zande L, Beukeboom LW. Hybrid incompatibilities in the parasitic wasp genus Nasonia: negative effects of hemizygosity and the identification of transmission ratio distortion loci. *Heredity* 2012; **108**: 302–311.

12   Lee H-Y, Chou J-Y, Cheong L, Chang N-H, Yang S-Y, Leu J-Y. Incompatibility of nuclear and mitochondrial genomes causes hybrid sterility between two yeast species. *Cell* 2008; **135**: 1065–1073.

13   Chou J-Y, Hung Y-S, Lin K-H, Lee H-Y, Leu J-Y. Multiple molecular mechanisms cause reproductive isolation between three yeast species. *PLoS Biol* 2010; **8**: e1000432.

14   Morales HE, Pavlova A, Amos N, Major R, Kilian A, Greening C *et al.* Concordant divergence of mitogenomes and a mitonuclear gene cluster in bird lineages inhabiting different climates. *Nat Ecol Evol* 2018; **2**: 1258–1267.

15   Moran BM, Payne CY, Powell DL, Iverson ENK, Banerjee SM, Madero A *et al.* A Lethal Genetic Incompatibility between Naturally Hybridizing Species in Mitochondrial Complex I. bioRxiv. 2022; : 2021.07.13.452279.

16   Baris TZ, Wagner DN, Dayan DI, Du X, Blier PU, Pichaud N *et al.* Evolved genetic and phenotypic differences due to mitochondrial-nuclear interactions. *PLoS Genet* 2017; **13**: e1006517.

17   Ellison CK, Burton RS. Cytonuclear conflict in interpopulation hybrids: the role of RNA polymerase in mtDNA transcription and replication. *J Evol Biol* 2010; **23**: 528–538.

18   Ellison CK, Burton RS. Genotype-dependent variation of mitochondrial transcriptional profiles in interpopulation hybrids. *Proc Natl Acad Sci U S A* 2008; **105**: 15831–15836.

19   Zaidi AA, Makova KD. Investigating mitonuclear interactions in human admixed populations. *Nat Ecol Evol* 2019; **3**: 213–222.

20   Wei W, Tuna S, Keogh MJ, Smith KR, Aitman TJ, Beales PL *et al.* Germline selection shapes human mitochondrial DNA diversity. *Science* 2019; **364**. doi:10.1126/science.aau6520.

21   López-Otín C, Blasco MA, Partridge L, Serrano M, Kroemer G. The hallmarks of aging. *Cell* 2013; **153**: 1194–1217.

22   Jónsson H, Sulem P, Kehr B, Kristmundsdottir S, Zink F, Hjartarson E *et al.* Parental influence on human germline de novo mutations in 1,548 trios from Iceland. *Nature* 2017; **549**: 519–522.

23   Rebolledo-Jaramillo B, Su MS-W, Stoler N, McElhoe JA, Dickins B, Blankenberg D *et al.* Maternal age effect and severe germ-line bottleneck in the inheritance of human mitochondrial DNA. *Proc Natl Acad Sci U S A* 2014; **111**: 15474–15479.

24   Linnane AW, Marzuki S, Ozawa T, M. T. Mitochondrial DNA mutations as an important contributor to ageing and degenerative diseases. *The Lancet* 1989. doi:10.1016/s0140-6736(89)92145-4.

25   Bogenhagen D, Clayton DA. The Number of Mitochondrial Deoxyribonucleic Acid Genomes in Mouse L and Human HeLa Cells: QUANTITATIVE ISOLATION OF MITOCHONDRIAL DEOXYRIBONUCLEIC ACID. *J Biol Chem* 1974; **249**: 7991–7995.

26   Filograna R, Mennuni M, Alsina D, Larsson N-G. Mitochondrial DNA copy number in human disease: the more the better? *FEBS Lett* 2021; **595**: 976–1002.

27   Sanchez-Contreras M, Kennedy SR. The Complicated Nature of Somatic mtDNA Mutations in Aging. *Front Aging* 2022; **2**. doi:10.3389/fragi.2021.805126.

28   López-Otín C, Blasco MA, Partridge L, Serrano M, Kroemer G. Hallmarks of aging: An expanding universe. *Cell* 2022. doi:10.1016/j.cell.2022.11.001.

29   Wallace DC. Mitochondrial diseases in man and mouse. *Science* 1999; **283**: 1482–1488.

30   Schmitt MW, Kennedy SR, Salk JJ, Fox EJ, Hiatt JB, Loeb LA. Detection of ultra-rare mutations by next-generation sequencing. *Proc Natl Acad Sci U S A* 2012; **109**:
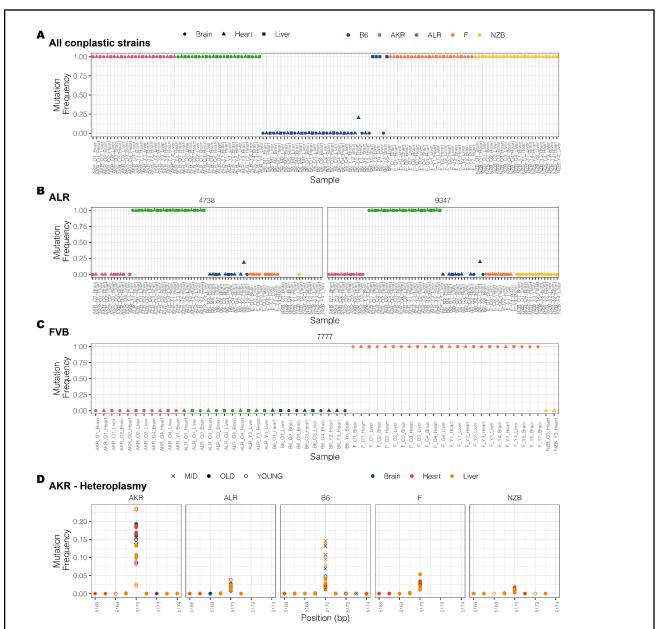
14508–14513.

31   Kennedy SR, Salk JJ, Schmitt MW, Loeb LA. Ultra-sensitive sequencing reveals an age-related increase in somatic mitochondrial mutations that are inconsistent with oxidative damage. *PLoS Genet* 2013; **9**: e1003794.

32   Arbeithuber B, Hester J, Cremona MA, Stoler N, Zaidi A, Higgins B *et al.* Age-related accumulation of de novo mitochondrial mutations in mammalian oocytes and somatic tissues. *PLoS Biol* 2020; **18**: e3000745.

33   Arbeithuber B, Cremona MA, Hester J, Barrett A, Higgins B, Anthony K *et al.* Advanced age increases frequencies of de novo mitochondrial mutations in macaque oocytes and somatic tissues. *Proc Natl Acad Sci U S A* 2022; **119**: e2118740119.

34   Sanchez-Contreras M, Sweetwyne MT, Tsantilas KA, Whitson JA, Campbell MD, Kohrn BF *et al.* The multi-tissue landscape of somatic mtdna mutations indicates tissue specific accumulation and removal in aging. *Elife* 2023; **12**: e83395.

35   Yu X, Gimsa U, Wester-Rosenlöf L, Kanitz E, Otten W, Kunz M *et al.* Dissecting the effects of mtDNA variations on complex traits using mouse conplastic strains. *Genome Res* 2009; **19**: 159–165.

36   Wanrooij S, Miralles Fusté J, Stewart JB, Wanrooij PH, Samuelsson T, Larsson N-G *et al.* In vivo mutagenesis reveals that OriL is essential for mitochondrial DNA replication. *EMBO Rep* 2012; **13**: 1130–1137.

37   Quigley GJ, Rich A. Structural Domains of Transfer RNA Molecules. *Science* 1976; **194**: 796–806.

38   Moreno-Loshuertos R, Pérez-Martos A, Fernández-Silva P, Enríquez JA. Length variation in the mouse mitochondrial tRNA(Arg) DHU loop size promotes oxidative phosphorylation functional differences. *FEBS J* 2013; **280**: 4983–4998.

39   Alexandrov LB, Nik-Zainal S, Wedge DC, Aparicio SAJR, Behjati S, Biankin AV *et al.* Signatures of mutational processes in human cancer. *Nature* 2013; **500**: 415–421.

40   Duncan BK, Miller JH. Mutagenic deamination of cytosine residues in DNA. *Nature* 1980; **287**: 560–561.

41   Zheng W, Khrapko K, Coller HA, Thilly WG, Copeland WC. Origins of human mitochondrial point mutations as DNA polymerase gamma-mediated errors. *Mutat Res* 2006; **599**: 11–20.

42   Cheng KC, Cahill DS, Kasai H, Nishimura S, Loeb LA. 8-Hydroxyguanine, an abundant form of oxidative DNA damage, causes G-T and A-C substitutions. *J Biol Chem* 1992; **267**: 166–172.

43   Gori K, Baez-Ortega A. sigfit: flexible Bayesian inference of mutational signatures. bioRxiv. 2020; : 372896.

44   Cagan A, Baez-Ortega A, Brzozowska N, Abascal F, Coorens THH, Sanders MA *et al.* Somatic mutation rates scale with lifespan across mammals. *Nature* 2022; **604**: 517–524.

45   Williams SL, Mash DC, Züchner S, Moraes CT. Somatic mtDNA mutation spectra in the

aging human putamen. *PLoS Genet* 2013; **9**: e1003990.

46   Li M, Schröder R, Ni S, Madea B, Stoneking M. Extensive tissue-related and allele-related mtDNA heteroplasmy suggests positive selection for somatic mutations. *Proceedings of the National Academy of Sciences* 2015; **112**: 2491–2496.

47   Li M, Schönberg A, Schaefer M, Schroeder R, Nasidze I, Stoneking M. Detecting heteroplasmy from high-throughput sequencing of complete human mitochondrial DNA genomes. *Am J Hum Genet* 2010; **87**: 237–249.

48   Samuels DC, Li C, Li B, Song Z, Torstenson E, Boyd Clay H *et al.* Recurrent tissue-specific mtDNA mutations are common in humans. *PLoS Genet* 2013; **9**: e1003929.

49   Moreno-Loshuertos R, Acín-Pérez R, Fernández-Silva P, Movilla N, Pérez-Martos A, de Cordoba SR *et al.* Differences in reactive oxygen species production explain the phenotypes associated with common mouse mitochondrial DNA variants. *Nat Genet* 2006; **38**: 1261–1268.

50   Zaidi AA, Wilton PR, Su MS-W, Paul IM, Arbeithuber B, Anthony K *et al.* Bottleneck and selection in the germline and maternal age influence transmission of mitochondrial DNA in human pedigrees. *Proc Natl Acad Sci U S A* 2019; **116**: 25172–25178.

51   Anik MI, Mahmud N, Masud AA, Khan MI, Islam MN, Uddin S *et al.* Role of Reactive Oxygen Species in Aging and Age-Related Diseases: A Review. *ACS Appl Bio Mater* 2022; **5**: 4028–4054.

52   Jastroch M, Divakaruni AS, Mookerjee S, Treberg JR, Brand MD. Mitochondrial proton and electron leaks. *Essays Biochem* 2010; **47**: 53–67.

53   Hirose M, Schilf P, Gupta Y, Wright MN, Wright MN, Jöhren O *et al.* Lifespan effects of mitochondrial mutations. *Nature* 2016; **540**: E13–E14.

54   Laslett D, Canbäck B. ARWEN: a program to detect tRNA genes in metazoan mitochondrial nucleotide sequences. *Bioinformatics* 2008; **24**: 172–175.

Supplementary Figures

Fig S1

Fig S1: Validation of conplastic strains. The mutation frequency, calculated as the number of alternative alleles divided by the number of duplex mt-genomes at the position, was checked for each haplotype site. (A) The mutation frequency for the T>C mutation at position 9460 in the gene *mt-ND3*. All conplastic strains differ from B6 (blue) at this position. B6 young liver samples that had this haplotype present were excluded from the study due to potential contamination. (B) The mutation frequency for ALR (green) haplotype sites positions 4738 (*mt-ND2*) and 9347 (*mt-COXIII*). The B6 young heart sample with presence of this haplotype was excluded from the study due to potential contamination. (C) The mutation frequency for the FVB (orange) haplotype site at position 7777 (*mt-Atp8*). (D) Comparison of the heteroplasmic allele frequency in the *OriL*. As expected, AKR has the highest heteroplasmic allele frequency compared to other strains including B6.

Fig S2

Fig S2: Proportion of alleles in the tRNA[Arg] 8 base mutation peak region. The proportion of each allele present in the A repeat region of the DHU arm of *mt-tRNA[Arg]* was calculated as the total number of each mutation type divided by the total number of mutations that occur in this region. This proportion was calculated for each experimental condition. Mutations that occur at a frequency > 1×10^{-3} were excluded from the analysis, including the previously known heteroplasmic frequency in *mt-tRNA[Arg]* across conplastic strains[35]. The mutation key (REF>ALT) denotes the mutation that occurs in *mt-tRNA[Arg]*, Ns in the ALT allele represent bases where a duplex consensus could not be reached.

Fig S3

Fig S3: Computationally predicted changes in tRNA^Arg structures. Structures were created using ARWEN (v1.2) [54]. Structures were created for the 3 most abundant mutation types across conditions (Fig S2): 1-3 A insertion in the DHU A-repeat region. As were inserted at position 9819 since we lack the resolution to locate the exact position an A-insertion occurs.

Fig S4

Fig S4: Change in SNVs, deletions, and insertions with age across all tissues. The average mutation frequency is compared between mt-haplotypes for different classes of mutations: single nucleotide variants (SNVs), deletions, and insertions. The average mutation frequency was calculated as the total mutation count in a class divided by the total duplex bp depth.

Fig S5

Fig S5: Estimation of the optimal number of mutational signatures. Observed counts for each mutation type were used for signature extraction using sigfit. A range of signatures (1-7) was given for possible signature extraction. Sigfit highlights the best number of signatures (as shown in red; signatures = 2), based on a cosine similarity metric that compares the original catalog of mutational signatures and the sigfit inferred signatures, as previously described in [43].

Fig S6

Fig S6: Mutation frequencies for macaque and mouse tissues in aged mice. The average frequency for point mutations was calculated as the total count of mutations of the given type divided by the duplex bp depth for the reference nucleotide. These average mutation frequencies were then normalized to the G>A/C>T mutation type, which is consistently the most abundant. Mutations with a frequency > 1x10^{-3} were excluded from this analysis. (A) The normalized average mutation frequency for the three most abundant mutations in this study across all experimental conditions. (B) The normalized average mutation frequency across three mouse tissues in Arbeithuber et al. 2020 [32]. (C) The normalized average mutation frequency across macaque tissues in Arbeithuber el al. 2022 [33].
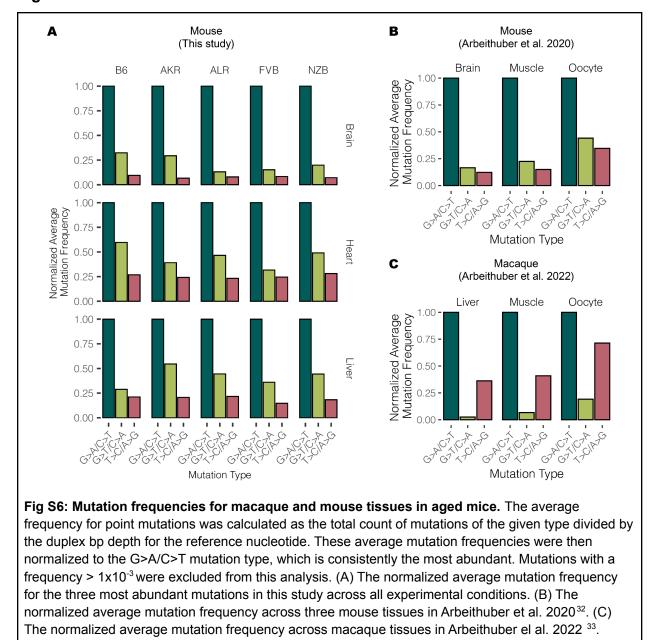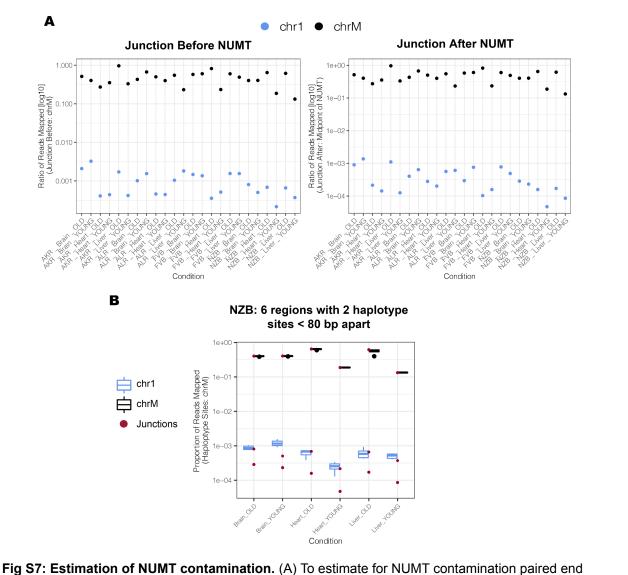
Fig S7

Fig S7: Estimation of NUMT contamination. (A) To estimate for NUMT contamination paired end duplex sequencing reads were remapped to mm10 with an unmasked chr1 NUMT. The number of reads that map to 10 bp upstream and 10 bp downstream of the NUMT region, referred to as the junction regions, was calculated. The figures denote the number of duplex reads that map to the junction regions divided by the average duplex depth of the corresponding region in the mt-genome with the chr1 NUMT masked (blue). Shown is also the number of reads that map to the corresponding junction regions in the mt-genome divided by the average duplex depth of the corresponding region in the mt-genome with the chr1 NUMT masked (black). (B) Duplex sequencing reads for the NZB strain were remapped using a NZB reference mt-genome. Six clusters of haplotype sites (regions where more than one haplotype site exists in a read) were identified. The distribution of the proportion of reads mapping the chr1 and those mapping to the mt-genome are depicted in boxplots. The proportion of reads mapping to chr1 and the mt-genome at the junction sites (shown in A) are represented in red.